Electronic Supplementary Information (ESI)

Controllable Atomic Defect Engineering in Layered $Ni_xFe_{1-x}(OH)_2$ Nanosheets for Electrochemical Overall Water Splitting

Jiajia Ge,[a]† Jin You Zheng,[a]† Jiangwei Zhang,[c] Suyu Jiang,[a] Xiaomei Yu,[a] Lili Zhang,[a] Liming Wang,[a] Wei Ma,*[a,b] Zhen Zhou,*[a] Renzhi Ma[d]

[a]Engineering Research Center of Advanced Functional Material Manufacturing of Ministry of Education, School of Chemical Engineering, Zhengzhou University, Zhengzhou 450001, China.

[b]State Key Laboratory of Powder Metallurgy, Central South University, Changsha, China

[c]Dalian National Laboratory for Clean Energy & State Key Laboratory of Catalysis, Dalian Institute of Chemical Physics, Chinese Academy of Sciences (CAS) Dalian 116023, China.

[d]International Center for Materials Nanoarchitectonics (MANA), National Institute for Materials Science (NIMS), Namiki 1-1, Tsukuba, Ibaraki, 305-0044, Japan.

†Both authors contributed equally.

Email: mawei@zzu.edu.cn; zhenzhou@zzu.edu.cn

Material Synthesis

Oxidization of multi-walled carbon nanotubes (MWCNTs): In a modified Hummer's method, 1.0 g MWCNTs and 0.3 g KNO_3 were dispersed in 50 ml concentrated sulfuric acid in a 1000 ml flask. Whereafter, 1.0 g $KMnO_4$ was slowly added and with 6 h of vigorous stirring at room temperature. After that, 30 ml deionized water was added dropwise to the mixture while keeping the temperature below 80°C. And then, 200 ml deionized water and 2.0 ml H_2O_2 were added to the beaker, the solution was kept stirring for 1 h. The final product was collected by centrifugation, washed repeatedly with deionized water until the pH reached ~ 5, and then lyophilized.

Preparation of defect-rich Ni_xFe_{1-x} hydroxides carbon nanotube complexes ($Ni_xFe_{1-x}(OH)_2$/CNT-t (t-oxidation time)): $Ni_xFe_{1-x}(OH)_2$/CNT-t was fabricated by a simple hydrothermal method and oxidation process. Briefly, 10 mg of oxidized MWCNTs was dissolved in 40 ml deionized water (with nitrogen gas protection for 2 h) assisted by sonication for 30 min. Thereafter, 0.3 mmol the total molar amount of $NiCl_2 \cdot 6H_2O$ and $FeCl_2 \cdot 4H_2O$ (the molar ratios were adjusted to 1:1, 2:1, and 3:1), ammonium fluoride (0.6 mmol), and hexamethylenetetramine (HMT, 2.0 mmol) were dissolved in the obtained solution and then transferred into a 100 ml Teflon lined stainless steel autoclave for a hydrothermal reaction at 120 °C for 6 h. After cooling naturally, the black product was collected, washed repeatedly with deionized water, and subsequently dispersed in a 50 ml mixed solution with a volume ratio of H_2O_2:H_2O=1:1 and magnetic stirring at room temperature for 0 h, 6 h, 24 h, and 36 h, respectively. The final products were collected, repetitively washed with deionized water and ethanol, and dried at ambient temperature with nitrogen gas protection. The final products are named $Ni_xFe_{1-x}(OH)_2$/CNT-t (t-oxidation time).

Synthesis of samples of $Ni_{1/2}Fe_{1/2}(OH)_2$-0 nanoplate, $Ni_{1/2}Fe_{1/2}(OH)_2$-24 nanoplate, and $Ni(OH)_2$/CNT-24 nanoplate: The other samples were synthesized by similar procedures of $Ni_xFe_{1-x}(OH)_2$/CNT-t synthesis with different precursors and oxidation time. $Ni_{1/2}Fe_{1/2}(OH)_2$-0 nanoplate was synthesized with 0.15 mmol of $NiCl_2 \cdot 6H_2O$

and 0.15 mmol $FeCl_2 \cdot 4H_2O$ (without oxidized MWCNTs and oxidation process). $Ni_{1/2}Fe_{1/2}(OH)_2$-24 nanoplate was synthesized with 0.15 mmol of $NiCl_2 \cdot 6H_2O$ and 0.15 mmol $FeCl_2 \cdot 4H_2O$ (without oxidized MWCNTs). $Ni(OH)_2$/CNT-24 nanoplate was synthesized with 0.3 mmol of $NiCl_2 \cdot 6H_2O$ (without $FeCl_2 \cdot 4H_2O$).

Material Characterization: The SEM of the obtain nanomaterials was collected by an FEI nano450. TEM, HRTEM, SAED, and element mapping images were characterized by an FEI Talos F200S with an accelerating voltage of 100 kV. The powder XRD test was performed on a Bruker D8 Advance X-ray diffractometer with a Cu Kα source. XPS measurements were recorded using an ESCALAB 250 instrument (Thermo Electron) with an Al Kα radiation.

XAFS measurements: The X-ray absorption fine structure spectra Ni K-edge were collected at laboratory X-ray spectrometer easy XAFS300+. The data were collected in transmission mode while the corresponding reference sample were collected in transmission mode at BL14W1 beamline of Shanghai Synchrotron Radiation Facility (SSRF) Shanghai. The sample was grinded and uniformly daubed on the special adhesive tape.

XAFS Analysis and Results: The acquired EXAFS data were processed according to the standard procedures using the ATHENA module of Demeter software packages.

The EXAFS spectra were obtained by subtracting the post-edge background from the overall absorption and then normalizing with respect to the edge-jump step. Subsequently, the χ(k) data of were Fourier transformed to real (R) space using hanging windows (dk=1.0 $Å^{-1}$) to separate the EXAFS contributions from different coordination shells. To obtain the quantitative structural parameters around central atoms, least-squares curve parameter fitting was performed using the ARTEMIS module of Demeter software packages

The following EXAFS equation was used:

$$\chi(k) = \sum_j \frac{N_j S_0^2 F_j(k)}{kR_j^2} \cdot \exp\left[-2k^2\sigma_j^2\right] \cdot \exp\left[\frac{-2R_j}{\lambda(k)}\right] \cdot \sin\left[2kR_j + \phi_j(k)\right]$$

the theoretical scattering amplitudes, phase shifts, and the photoelectron mean free path for all paths calculated. S_0^2 is the amplitude reduction factor, $F_j(k)$ is the effective

curved-wave backscattering amplitude, N_j is the number of neighbors in the j^{th} atomic shell, R_j is the distance between the X ray absorbing central atom and the atoms in the j^{th} atomic shell (backscatterer), λ is the mean free path in Å, $\phi_j(k)$ is the phase shift (including the phase shift for each shell and the total central atom phase shift), σ_j is the Debye-Waller parameter of the j^{th} atomic shell (variation of distances around the average R_j). The functions $F_j(k)$, λ and $\phi_j(k)$ were calculated with the ab initio code FEFF9. The additional details for EXAFS simulations are given below.

All fits were performed in the *R* space with a *k*-weight of 2 while phase correction was also applied in the first coordination shell to make the R value close to the physical interatomic distance between the absorber and shell scatterer. The coordination numbers of model samples were fixed as the nominal values. While S_0^2, the internal atomic distances R, Debye-Waller factor σ^2, and the edge-energy shift Δ were allowed to run freely.

In-situ **Raman spectroelectrochemical study:** The *in-situ* Raman spectra of nanomaterials were recorded on the LabRAM HR Evolution Raman spectrometer with an excitation wavelength of 532 nm. The prepared catalysts, platinum wire, and Ag/AgCl (containing saturated KCl) were served as the working, counter, and reference electrodes, respectively. The electrolyte is a solution of 1.0 M KOH. During the current time (i-t) measurement, the in-situ Raman spectra of the working electrode were recorded at different potentials with a 60 s acquisition time, ranging from 100 to 900 cm^{-1}. The applied potential is gradually increased from 1.13 V to 1.53 V (vs RHE) at 0.1 V intervals. In each step, a potential of five minutes is applied.

Electrochemical measurements: For OER and HER measurements, the electrochemical studies of these catalysts were assessed on a CHI 760E electrochemical workstation with a three-electrode setup in 1.0 M KOH solution at room temperature. First, 2.5 mg catalysts powers, 800 μL deionized water, 800 μL isopropanol, and 14 μL Nafion solution (10 wt%) were mixed to form a homogeneous ink by ultrasound for more than 30 min. Then, 9.6 μL slurry was coated on a glassy carbon electrode (3 mm diameter) as the working electrode (with a load of 0.21

mg/cm^2), platinum foil, and Ag/AgCl (with the saturated KCl) electrode as the counter and the reference electrode, respectively. All LSV curves were obtained by rotating the working electrode to move O_2 or H_2 at the scanning rate of 5 mV s^{-1} under the intense agitation of 1600 r/min after 10 cyclic voltammetry scanning activation, and all curves with 95% IR compensation. The EIS measurements were conducted in the frequency ranging from 1.0 Hz to 10^5 Hz. ECSA is calculated according to CV by the same disk electrodes at the potential range of 1.024-1.124 V (vs RHE). A series of CV curves were gained at different scan rates (20, 40, 60, 80, 100, and 120 mV/s). After plotting the difference of current density ($\Delta j = j_a - j_c$) at the potential of 1.074 V vs the scan rates, the slope, twice the C_{dl}, is normally used to represent the ECSA.

For overall water splitting measurement, the catalysts were assessed on a two-electrode electrolyzer in the same alkaline environment. First, 3.0 mg catalysts powers, 800 μL deionized water, 800 μL isopropanol, and 14 μL Nafion solution (10 wt%) were mixed to form a homogeneous ink by ultrasound for more than 30 min. Then, 230 μL slurry was coated on nickel foam (1×1 cm) as the working electrode (with a load of 0.21 mg/cm^2) and platinum foil as the counter electrode. All LSV curves were obtained at the scanning rate of 5 mV s^{-1} after 10 cyclic voltammetry scanning activation in the same alkaline environment. In order to assess the long-term stability of overall water splitting, the chronopotentiometry response was measured at a current density of 10 mA cm^{-2} for 12 h.

Photovoltaic-Electrocatalytic Water Splitting: The characterization of photovoltaic-water electrolysis was performed by online gas chromatography (GC-2014C, Shimadzu Corporation, Japan), the chromatograph was connected to a closed gas circulation system with a water separation reactor (online 3, Shanghai Boyi Scientific Instrument Co., China). Generally, the anode and cathode ($Ni_{1/2}Fe_{1/2}(OH)_2$/CNT-24 coated on the 1×1 cm Ni foam and the load is 2.0 mg/cm^2) are kept at a distance of 2 cm and installed on the water-splitting reactor, and then connected to the crystalline silicon solar cell. The electrolyte of water splitting is 1.0 M KOH, and the consumption is about 280 mL. The vacuum state of the water-splitting reactor and closed gas-circulation system was realized by vacuum treatment.

The light source is a Xe lamp (400 < λ <800 nm), and its intensity can be controlled by adjusting the input current of the Xe lamp and/or the distance from the light source to the solar cell. Crystalline silicon solar cells converted photo energy into electricity with a total radiation area of 14.4 cm^2. In order to prevent solar cells from overheating, a circulating water device is used. The voltage of the electrode is monitored by a voltmeter. After the Xe lamp is turned on, the working voltage of the solar cell is maintained at 2.4 V by adjusting the intensity of the light source.

Calculation of Solar-to-Hydrogen Energy Conversion Efficiency: The wavelength range of the Xe lamp intensity is concentrated in 400 ~ 800 nm (as shown in Fig. S20), and the average total light intensity is measured with a photometer is 0.27 μW cm^{-2}. The silicon solar cell with an irradiated area of 14.4 cm^2. The standard molar enthalpy of combustion for H_2 is -285.84 KJ mol^{-1}. In the first 1 h, the yield of H_2 was 5020.8 μmol. The specific calculation steps are as follows:

Input: Solar energy (J) = light intensity (W cm^{-2}) × illumination area (cm^2) × time (s) = 0.27 Wcm^{-2} × 14.4 cm^2 × 3600 s = 13996.8 J =13.9968 kJ

Output: H_2 energy (kJ) = standard molar enthalpy of combustion (kJ mol^{-1}) ×H_2 moles (mol) = 285.84 kJ mol^{-1} ×5020.8× 10^{-6} mol = 1.435 kJ

Solar-to-Hydrogen energy conversion efficiency = H_2 energy (kJ) / Solar energy (kJ) = 1.435 /13.997= 10.25%

Calculation of the Faraday Efficiency

Faraday efficiency is defined as the ratio of the actual amount of product to the theoretical amount. Divide the total charge ($Q = I \times t$) passed in the reaction by $n \times F$ (n is the number of electrons transferred and F is the Faraday constant) to obtain the theoretical gas yield. m refers to the actual moles of the product (5020.8 μmol in the first 1 h). The calculation formula of Faraday efficiency is as follows:

Faraday efficiency = actual gas yield / theoretical gas yield = $m/[(I \times t)/(n \times F)] = (m \times n \times F)/(I \times t)$ = (5020.8× 10^{-6} mol × 2 × 96485 C mol^{-1})/(273.1 × 10^{-3} A × 3600 s) = 98.55%

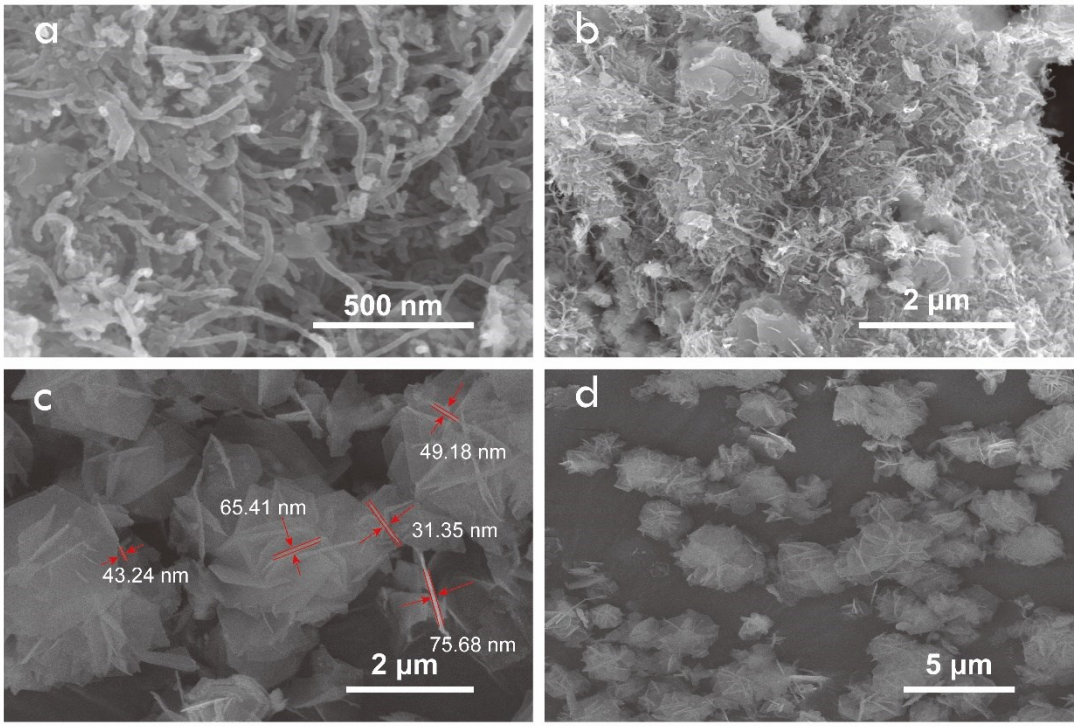

Fig. S1 SEM images of (a, b) $Ni_{1/2}Fe_{1/2}(OH)_2$/CNT-24 and (c, d) $Ni_{1/2}Fe_{1/2}(OH)_2$-24.

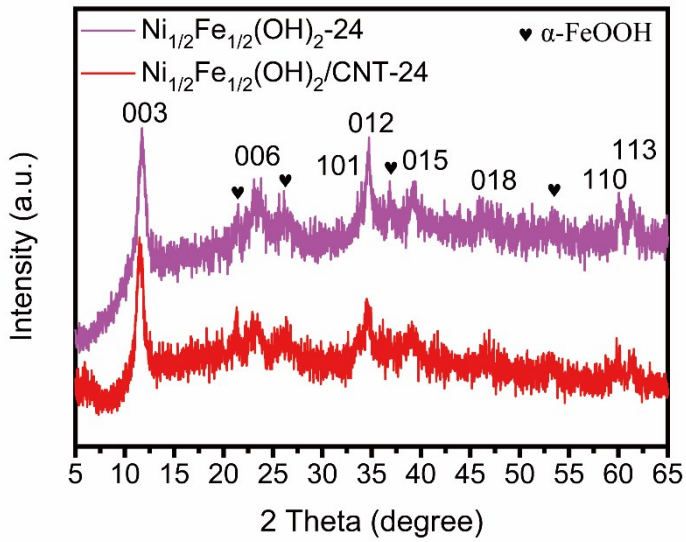

Fig. S2 XRD patterns of $Ni_{1/2}Fe_{1/2}(OH)_2$-24 and $Ni_{1/2}Fe_{1/2}(OH)_2$/CNT-24.

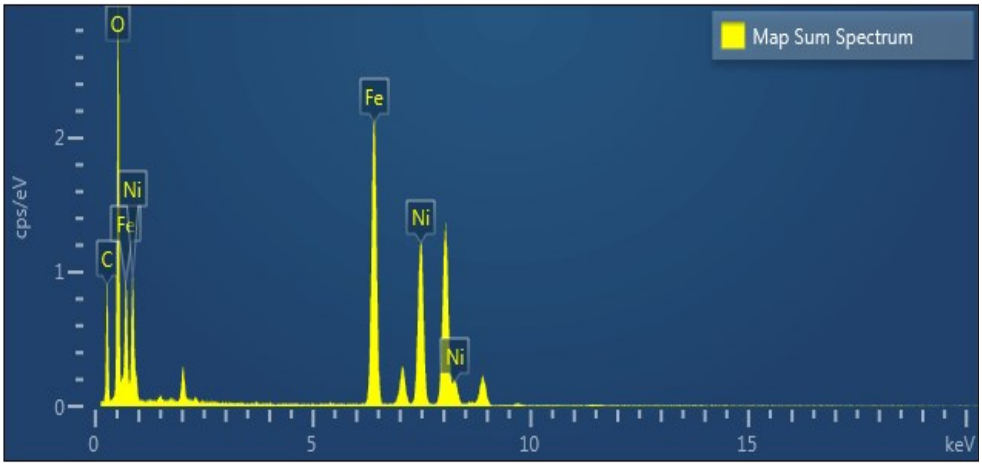

Fig. S3 EDS of $Ni_{1/2}Fe_{1/2}(OH)_2$/CNT-24 sample by TEM.

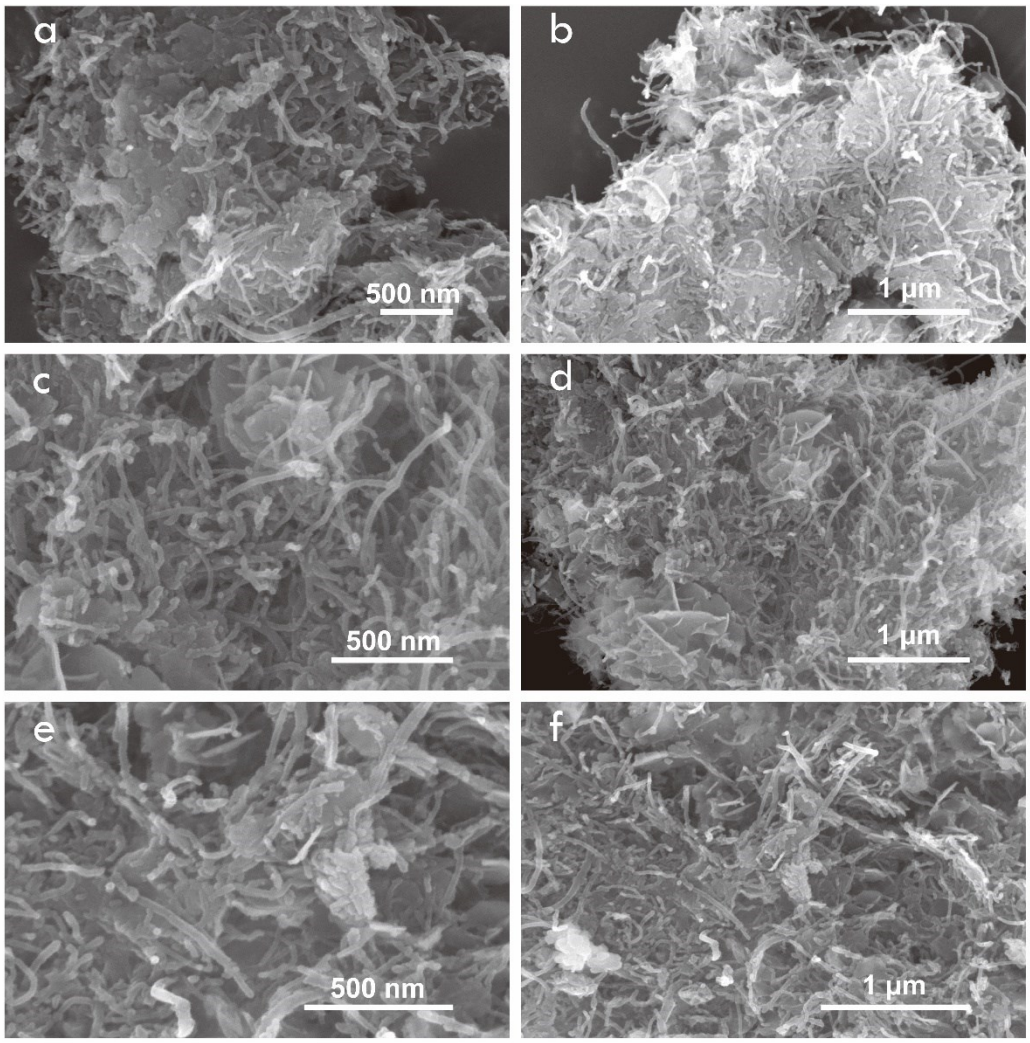

Fig. S4 SEM images of (a, b) $Ni_{1/2}Fe_{1/2}(OH)_2$/CNT-0, (c, d) $Ni_{1/2}Fe_{1/2}(OH)_2$/CNT-6, and (e, f) $Ni_{1/2}Fe_{1/2}(OH)_2$/CNT-36.

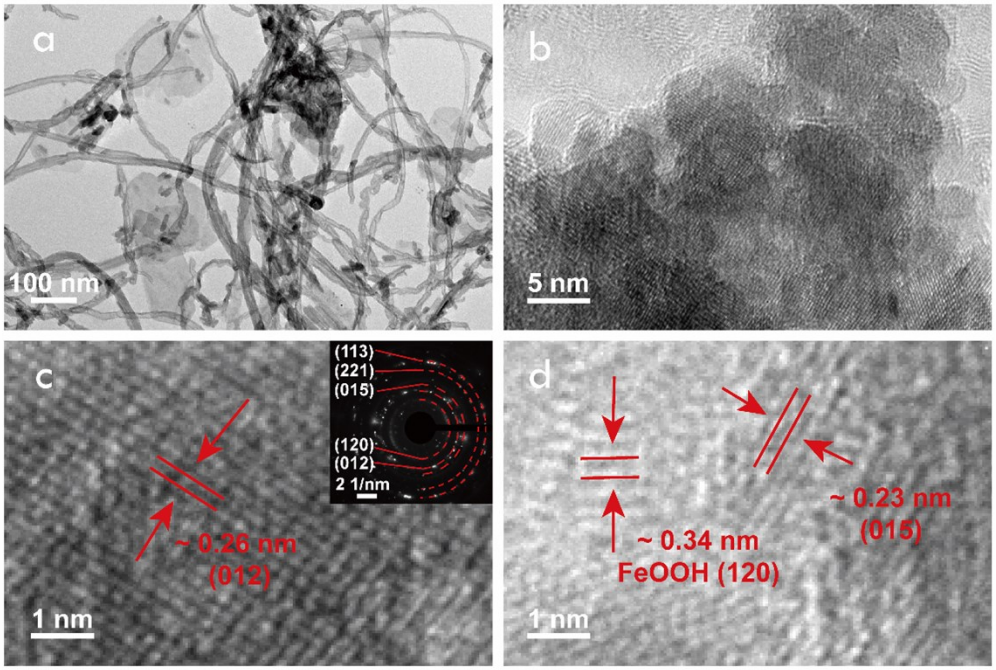

Fig. S5 TEM images of $Ni_{1/2}Fe_{1/2}(OH)_2$/CNT-0. (a) TEM image, (b-d) HRTEM images.

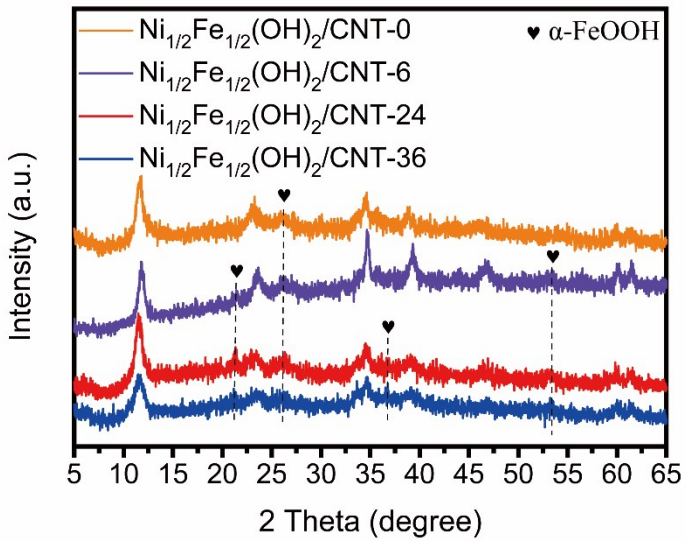

Fig. S6 XRD patterns of $Ni_{1/2}Fe_{1/2}(OH)_2$/CNT-0, $Ni_{1/2}Fe_{1/2}(OH)_2$/CNT-6, $Ni_{1/2}Fe_{1/2}(OH)_2$/CNT-24, and $Ni_{1/2}Fe_{1/2}(OH)_2$/CNT-36.

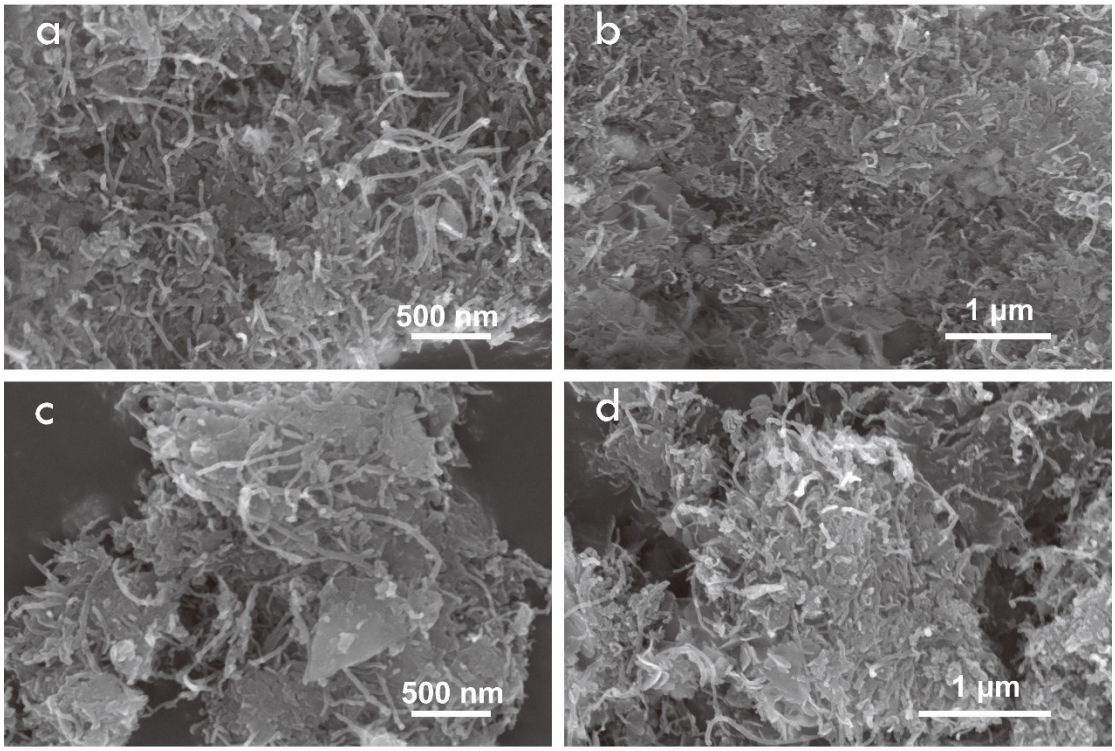

Fig. S7 SEM images of (a, b) $Ni_{2/3}Fe_{1/3}(OH)_2$/CNT-24 and (c, d) $Ni_{3/4}Fe_{1/4}(OH)_2$/CNT-24.

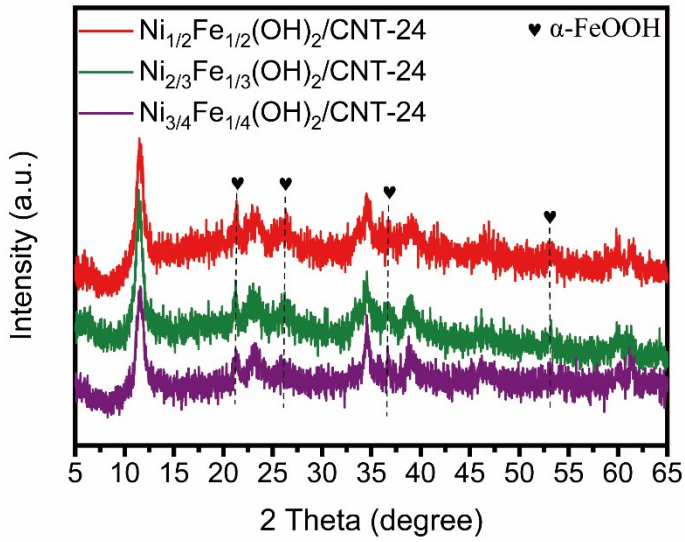

Fig. S8 XRD patterns of $Ni_xFe_{1-x}(OH)_2$/CNT-24 samples prepared with different ratios of Ni and Fe.

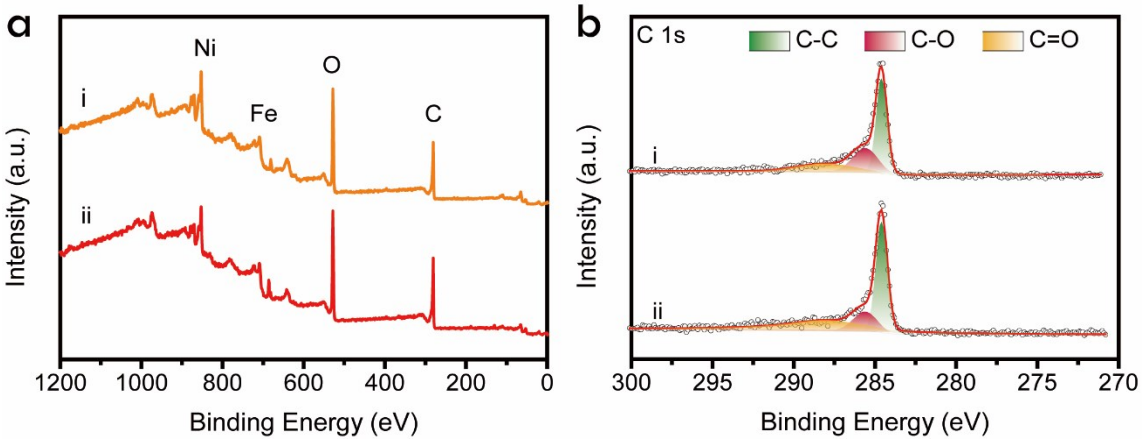

Fig. S9 The XPS patterns of the $Ni_{1/2}Fe_{1/2}(OH)_2$/CNT-0 (i) and $Ni_{1/2}Fe_{1/2}(OH)_2$/CNT-24 (ii). (a) XPS full-spectrum, (b) C1s.

Table S1. The ratio of Ni^{3+}:Ni^{2+}, and Fe^{3+}: Fe^{2+} in the surface of materials.

Catalyst	Ni^{3+}:Ni^{2+}	Fe^{3+}:Fe^{2+}
$Ni_{1/2}Fe_{1/2}(OH)_2$/CNT-0	0.18	0.11
$Ni_{1/2}Fe_{1/2}(OH)_2$/CNT-24	0.39	0.33

Table S2. The ratio of M-O:M-OH, O_V:M-OH, and H_2O:M-OH in the surface of materials.

Catalyst	M-O:M-OH	O_V:M-OH	H_2O:M-OH
$Ni_{1/2}Fe_{1/2}(OH)_2$/CNT-0	0.07	0.09	0.13
$Ni_{1/2}Fe_{1/2}(OH)_2$/CNT-24	0.13	0.21	0.11

Table S3. Local structure parameters around Ni estimated by EXAFS analysis.

Sample	Reduced Chi-square (χ_v^2)	R-Factor (%)	amp/S_0^2	Bond	N[a]	R[b](Å)	$\sigma^{2[c]}$ (10^{-3}Å^2)	ΔE_0 (eV)
$Ni_{1/2}Fe_{1/2}(OH)_2$ /CNT-24	3640.54	0.0391	1.02±0.15	Ni-O	4.5	2.073±0.012	4.8±2.2	2.11±1.41
			0.90±0.17	Ni-Fe (Ni-Ni)	4.0	3.114±0.018	6.7±3.2	-3.01±1.89

[a] N = coordination number

[b] R = distance between absorber and backscattering atoms

[c] σ^2 = Debye-Waller factor

Table S4. Comparison of the OER performance for $Ni_{1/2}Fe_{1/2}(OH)_2$/CNT-24 catalyst with other reported electrocatalysts in 1.0 M KOH.

Sample	Overpotential/mV	Tafel slope/mV dec^{-1}	Reference
$Ni_{1/2}Fe_{1/2}(OH)_2$/CNT-24	244	41	This Work
NiFe-LDH/CNT	247	31	1
Co-Bi NS/graphene	290	53	2
Co_3O_4	290	84	3
CoFe LDH-F	300	40	4
E-CoFe LDHs	302	41	5
NF-AC-NiO_x-Fe	245	34	6
Co(OH)F	313	53	7
Ni_3FeN	280	46	8

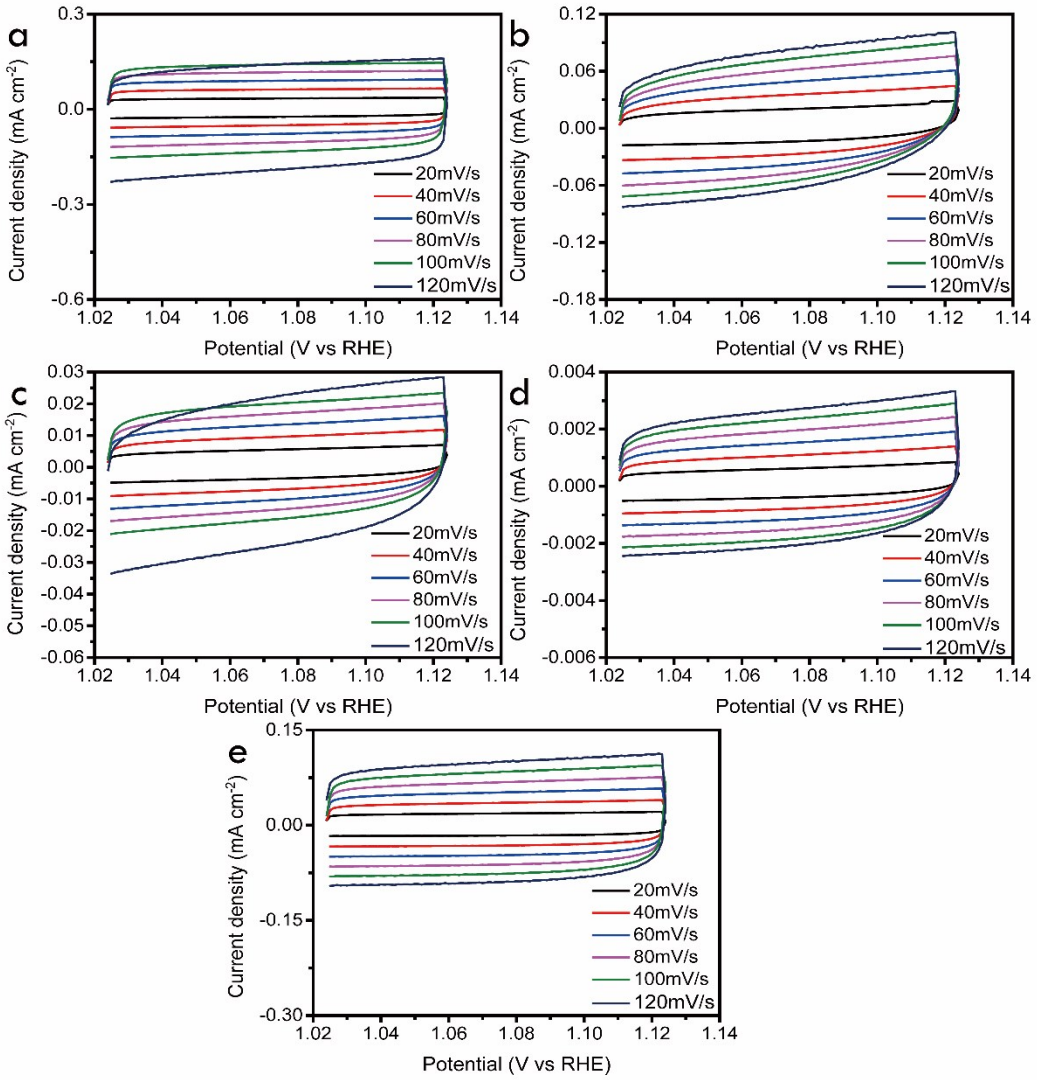

Fig. S10 CV of $Ni_{1/2}Fe_{1/2}(OH)_2$/CNT-24 (a), $Ni_{1/2}Fe_{1/2}(OH)_2$-24+CNT-24 (b), $Ni_{1/2}Fe_{1/2}(OH)_2$-24 (c),$Ni_{1/2}Fe_{1/2}(OH)_2$-0 (d), and RuO_2 (e).

Table S5. Optimum fitting results for $Ni_{1/2}Fe_{1/2}(OH)_2$/CNT-24 and the other samples.

Catalyst	R_s/Ω	R_f/Ω	$CPE_f/\mu Fcm^{-2}$	R_{ct}/Ω	$CPE_{dl}/\mu Fcm^{-2}$
$Ni_{1/2}Fe_{1/2}(OH)_2$/CNT-24	15.7	4.0	9009.4 (α= 0.52)	12.9	1824.2 (α= 0.95)
$Ni_{1/2}Fe_{1/2}(OH)_2$-24+CNT-24	15.5	46.9	739.6 (α= 0.54)	48.4	855.0 (α= 0.89)
$Ni_{1/2}Fe_{1/2}(OH)_2$-24	14.9	179.2	9.5 (α= 0.81)	306.9	125.6 (α= 0.72)
$Ni_{1/2}Fe_{1/2}(OH)_2$-0	14.7	174.1	34.7 (α= 0.75)	1356.0	43.9 (α= 0.70)
RuO_2	19.8	3.5	6095.3 (α= 0.57)	37.2	345.3 (α= 0.99)

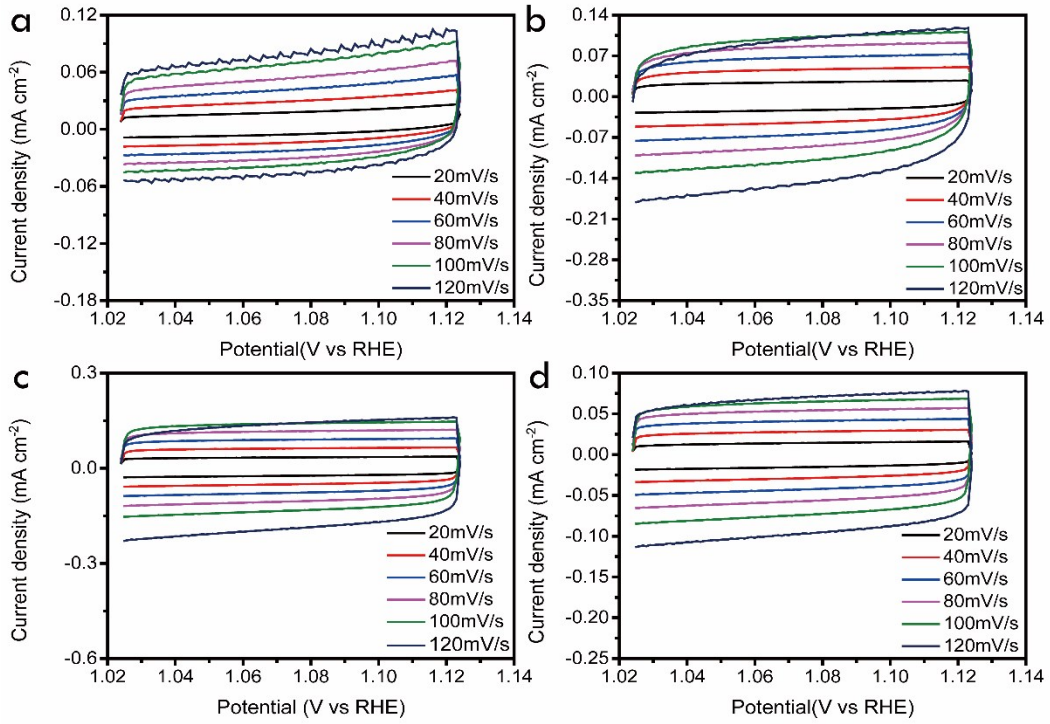

Fig. S11 CV of $Ni_{1/2}Fe_{1/2}(OH)_2$/CNT-0 (a), $Ni_{1/2}Fe_{1/2}(OH)_2$/CNT-6 (b), $Ni_{1/2}Fe_{1/2}(OH)_2$/CNT-24 (c), and $Ni_{1/2}Fe_{1/2}(OH)_2$/CNT-36 (d).

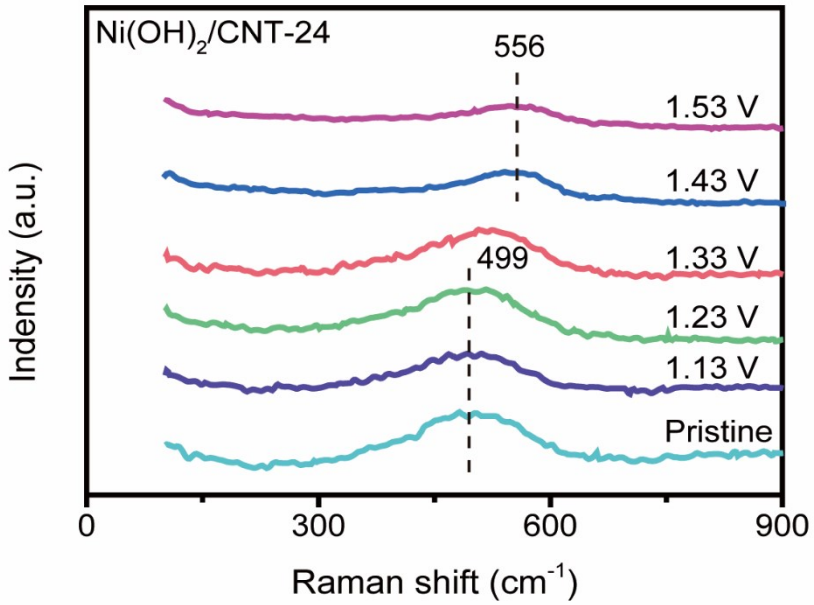

Fig. S12 *In-situ* Raman spectra under 1.0 M KOH conditions for different potentials of $Ni(OH)_2$/CNT-24.

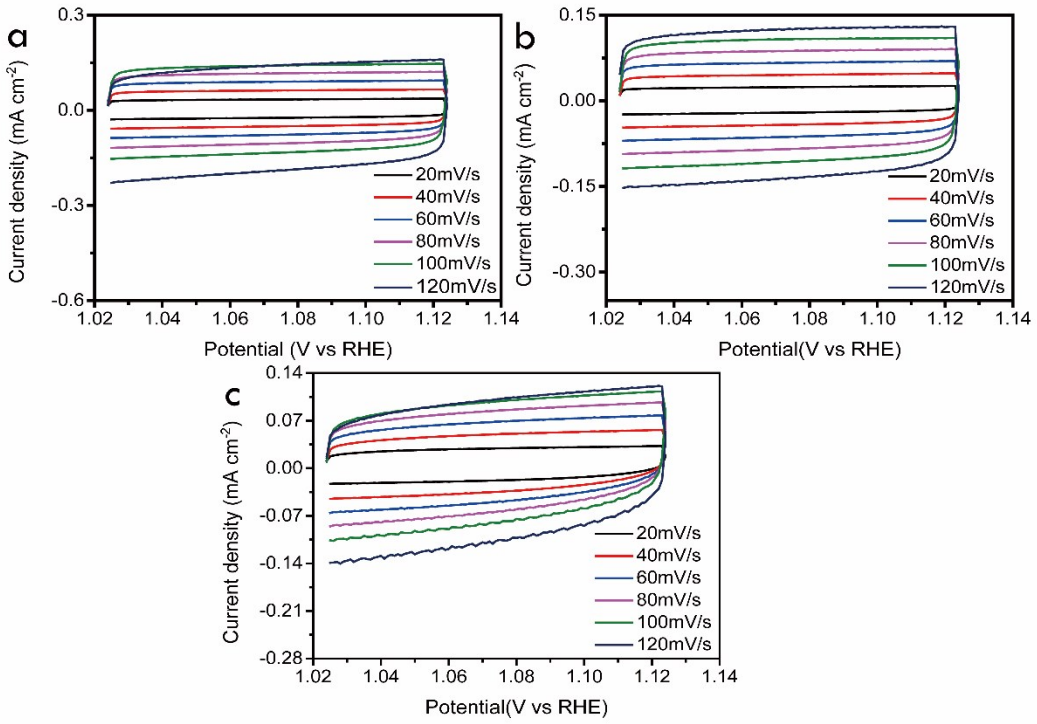

Fig. S13 CV of $Ni_{1/2}Fe_{1/2}(OH)_2$/CNT-24 (a), $Ni_{2/3}Fe_{1/3}(OH)_2$/CNT-24 (b), and $Ni_{3/4}Fe_{1/4}(OH)_2$/CNT-24 (c).

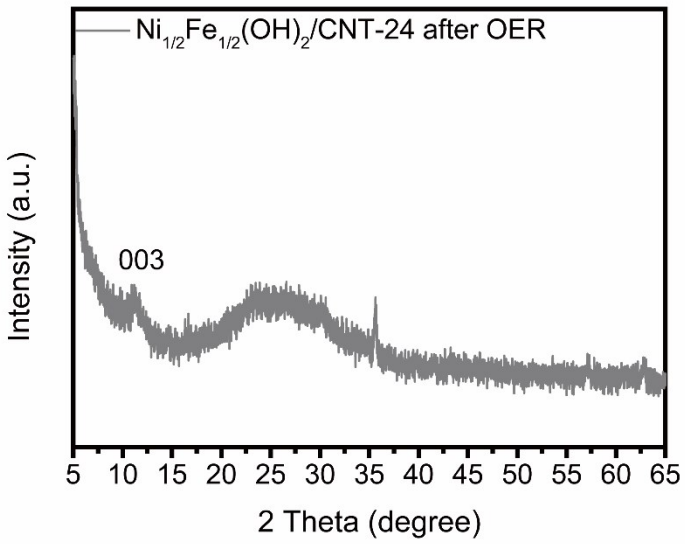

Fig. S14 XRD patterns of $Ni_{1/2}Fe_{1/2}(OH)_2$/CNT-24 after OER test.

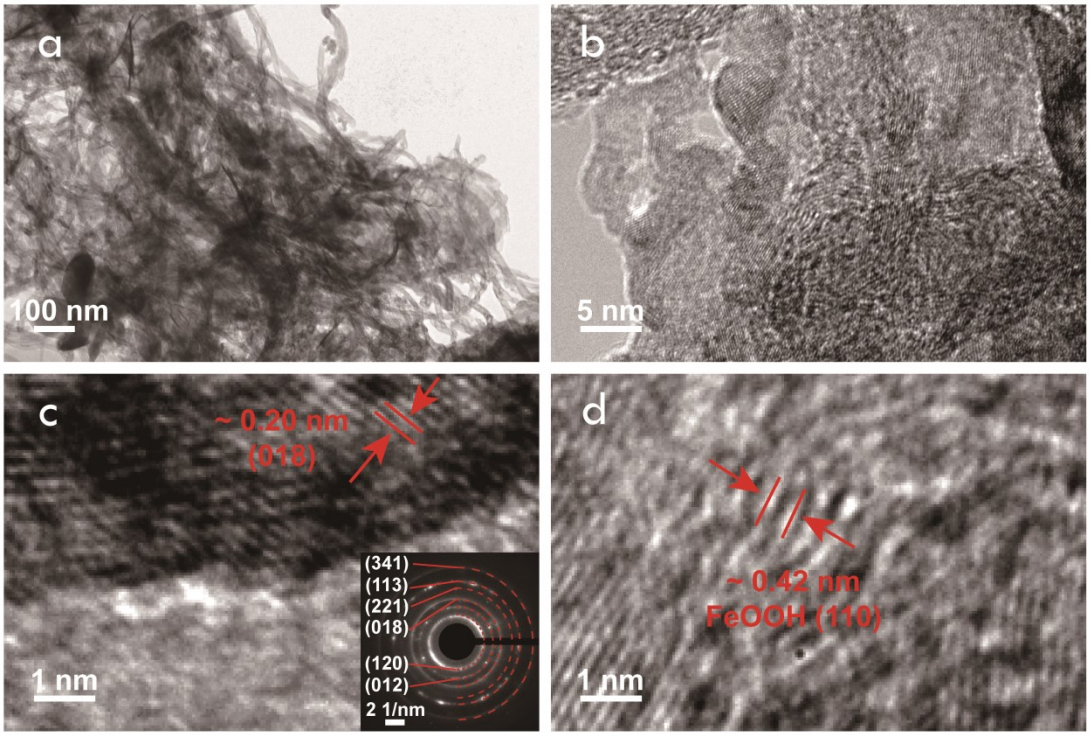

Fig. S15 The TEM images of $Ni_{1/2}Fe_{1/2}(OH)_2$/CNT-24 after OER test. (a) TEM image, (b-d) HRTEM images.

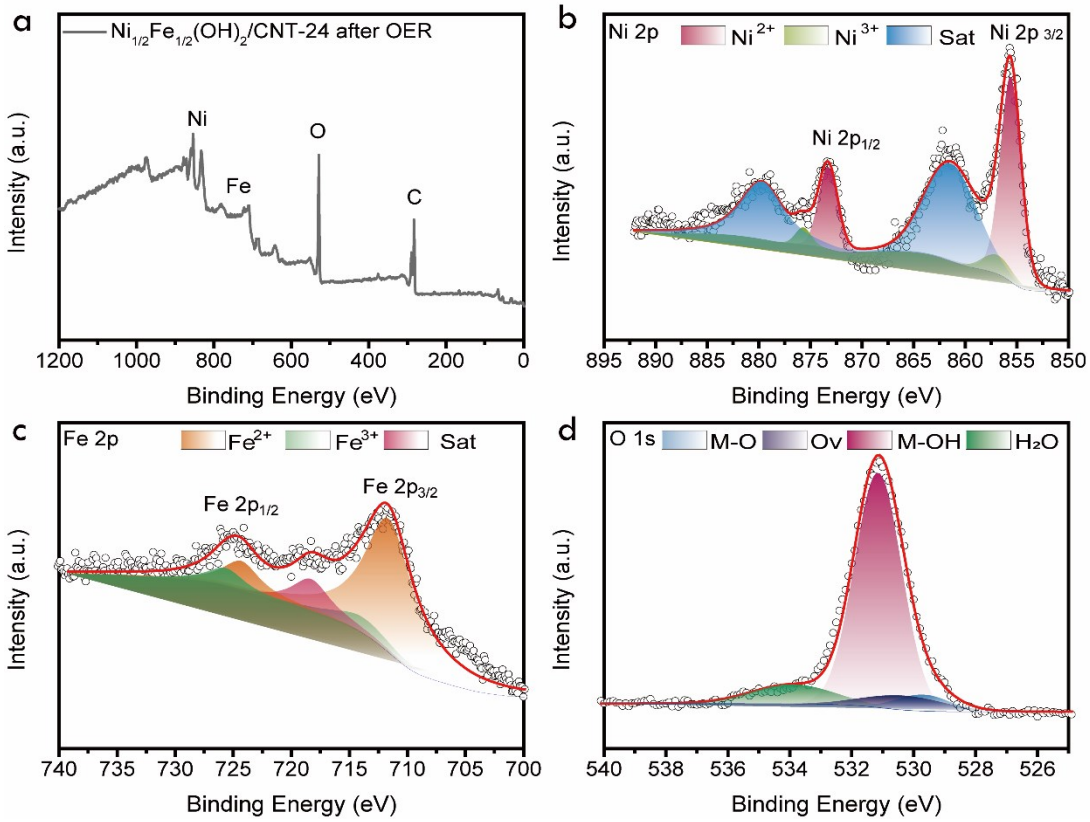

Fig. S16 The XPS of $Ni_{1/2}Fe_{1/2}(OH)_2$/CNT-24 after OER test. (a) full-spectrum, (b) Ni 2p, (c) Fe 2p, (d) O 1s.

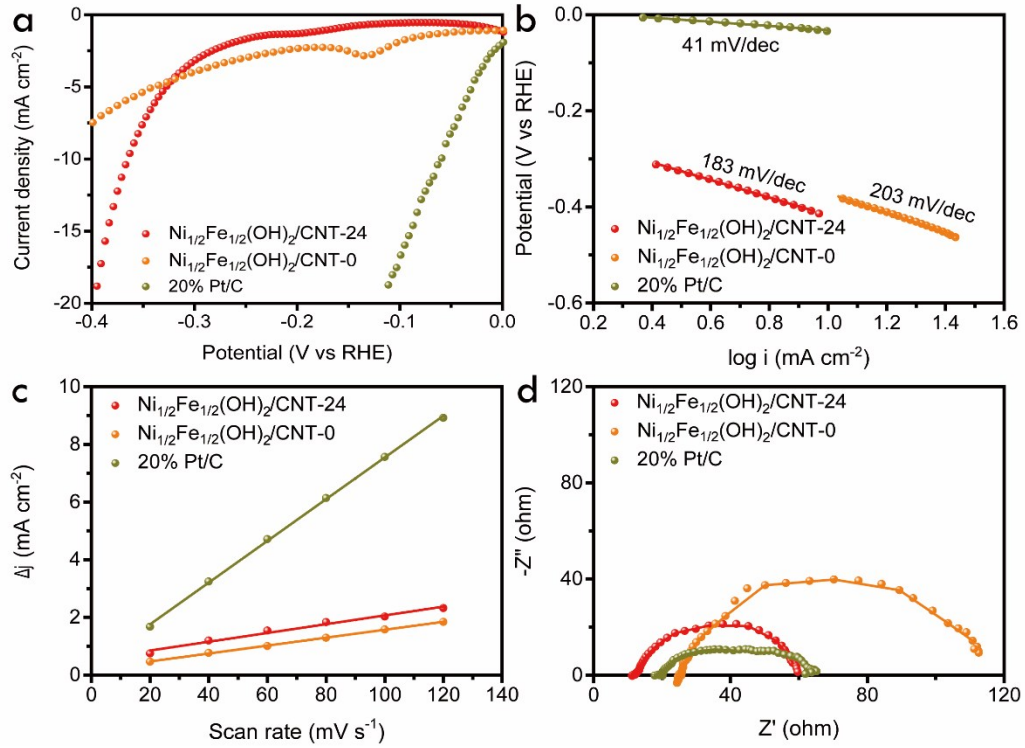

Fig. S17 (a) LSV curves, (b) Tafel slops, (c) ECSA, and (d) EIS of $Ni_{1/2}Fe_{1/2}(OH)_2$/CNT-24, $Ni_{1/2}Fe_{1/2}(OH)_2$/CNT-0, and 20% Pt/C for HER.

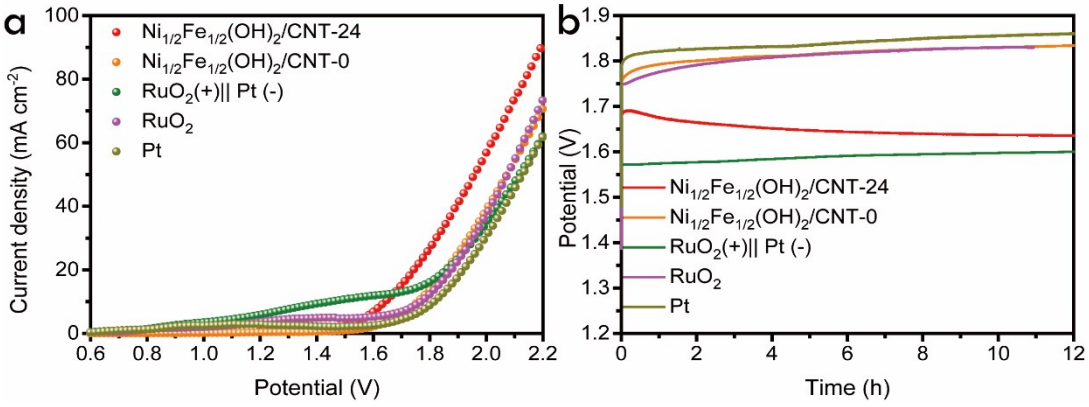

Fig. S18 (a) LSV curves and (b) CP of $Ni_{1/2}Fe_{1/2}(OH)_2$/CNT-24, $Ni_{1/2}Fe_{1/2}(OH)_2$/CNT-0, RuO_2 (+) || Pt/C (-), RuO_2, and Pt/C for overall water splitting.

Table S6. Comparison of the overall water splitting performance for $Ni_{1/2}Fe_{1/2}(OH)_2$/CNT-24 with other reported electrocatalysts at 10 mA cm^{-2} in 1.0 M KOH.

Catalysts	Load /mg cm^{-2}	Substrate	Potential /V	Reference
$Ni_{1/2}Fe_{1/2}(OH)_2$/CNT-24	0.21	Ni foam	1.64	This work
Ni_2P	5.0	Ni foam	1.63	9
Co-Mn carbonate hydroxide	5.6	Ni foam	1.68	10
NiCoP	1.6	Ni foam	1.58	11
EG/$Co_{0.85}$Se/NiFeLDH	4.0	graphite foil	1.67	12
Ni@NiFe LDH	2.3	Ni foam	1.53	13
NiFe LDH@NiCoP/NF	2.0	Ni foam	1.57	14

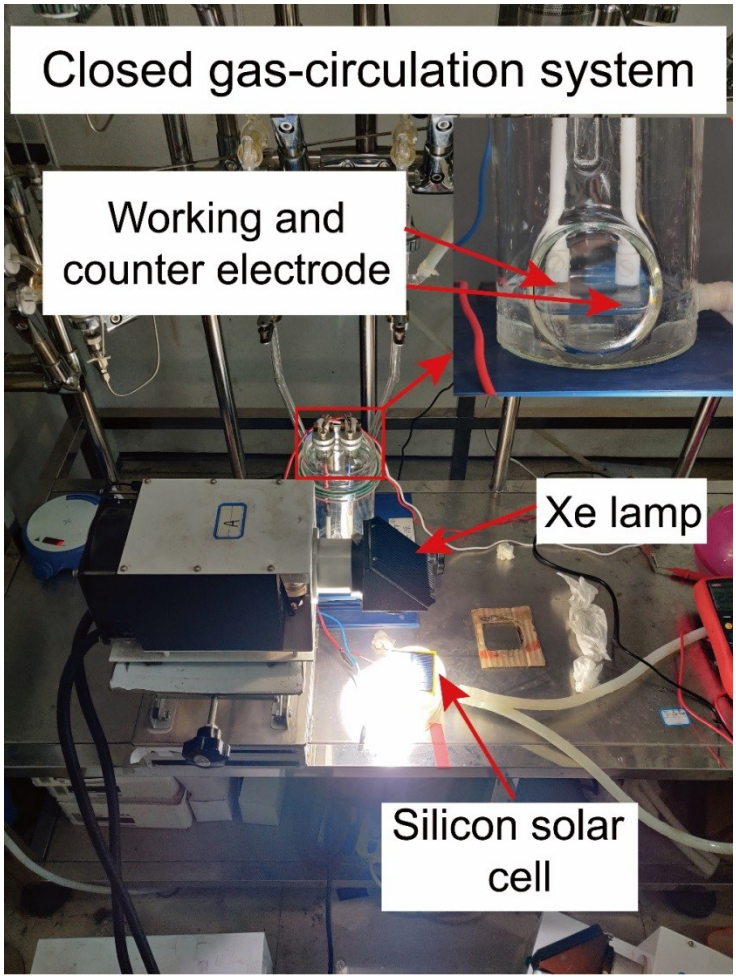

Fig. S19 The photograph of the photovoltaic-electrocatalytic water splitting system.

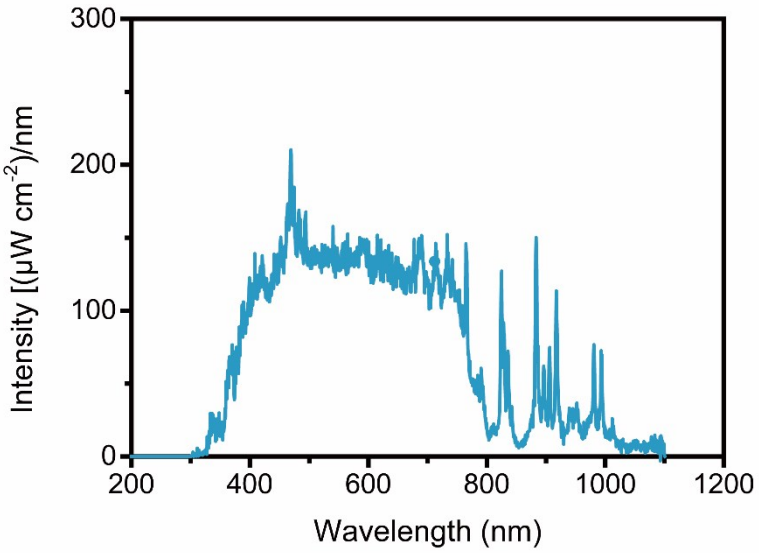

Fig. S20 Intensity spectrum of the Xe lamp (wavelength range of 400 nm < λ < 800 nm).

References

1. M. Gong, Y. Li, H. Wang, Y. Liang, J. Z. Wu, J. Zhou, J. Wang, T. Regier, F. Wei and H. Dai, *J. Am. Chem. Soc*., 2013, **135**, 8452-8455.
2. P. Chen, K. Xu, T. Zhou, Y. Tong, J. Wu, H. Cheng, X. Lu, H. Ding, C. Wu and Y. Xie, *Angew. Chem., Int. Edit*., 2016, **55**, 2488-2492.
3. Y. P. Zhu, T. Y. Ma, M. Jaroniec and S. Z. Qiao, *Angew. Chem., Int. Edit*., 2017, **56**, 1324-1328.
4. P. F. Liu, S. Yang, B. Zhang and H. G. Yang, *ACS Appl. Mater. Interfaces*, 2016, **8**, 34474-34481.
5. P. Zhou, Y. Wang, C. Xie, C. Chen, H. Liu, R. Chen, J. Huo and S. Wang, *Chem. Commun.*, 2017, **53**, 11778-11781.
6. F. Song, M. M. Busch, B. Lassalle-Kaiser, C.-S. Hsu, E. Petkucheva, M. Bensimon, H. M. Chen, C. Corminboeuf and X. Hu, *ACS Cent. Sci.*, 2019, **5**, 558-568.
7. S. Wan, J. Qi, W. Zhang, W. Wang, S. Zhang, K. Liu, H. Zheng, J. Sun, S. Wang and R. Cao, *Adv. Mater.*, 2017, **29**, 1700286.
8. X. Jia, Y. Zhao, G. Chen, L. Shang, R. Shi, X. Kang, G. I. N. Waterhouse, L.-Z. Wu, C.-H. Tung and T. Zhang, *Adv. Energy Mater.*, 2016, **6**, 1502585.
9. L. Stern, L. Feng, F. Song and X. Hu, *Energy Environ. Sci.*, 2015, **8**, 2347.
10. T. Tang, W. J. Jiang, S. Niu, N. Liu, H. Luo, Y. Y. Chen, S. F. Jin, F. Gao, L. J. Wan and J. S. Hu, *J. Am. Chem. Soc.*, 2017, **139**, 8320-8328.
11. H. Liang, A. N. Gandi, D. H. Anjum, X. Wang, U. Schwingenschlogl and H. N. Alshareef, *Nano Lett*., 2016, **16**, 7718-7725.
12. Y. Hou, M. R. Lohe, J. Zhang, S. Liu, X. Zhuang and X. Feng, *Energy Environ. Sci.*, 2016, **9**, 478-483.
13. Z. Cai, X. Bu, P. Wang, W. Su, R. Wei, J. C. Ho, J. Yang and X. Wang, *J. Mater. Chem. A*, 2019, **7**, 21722-21729.
14. H. Zhang, X. Li, A. Hähnel, V. Naumann, C. Lin, S. Azimi, S. L. Schweizer, A. W. Maijenburg and R. B. Wehrspohn, *Adv. Funct. Mater*., 2018, **28**, 1706847.